EURODINAME III - An International Symposium on Dynamic Problems of Mechanics
June 8-11, 2026 - Giens Peninsula, FR

EURODINAME-2026-13480
ON THE WAVE PROPAGATION IN HYDROELASTIC PERIODIC STRUCTURES: THEORY AND EXPERIMENTS

Vinícius Mauro de Souza Santos
Aeronautics Institute of Technology, Praça Marechal Eduardo Gomes, 50 – São José dos Campos, 12228-900, SP, Brazil
Université Marie et Louis Pasteur, SUPMICROTECH, CNRS, Institut FEMTO-ST, Besançon, F-25000, France
vinicius.santos@ga.ita.br, vinicius.mauro@femto-st.fr

Romain Viala
Université Marie et Louis Pasteur, SUPMICROTECH, CNRS, Institut FEMTO-ST, Besançon, F-25000, France
romain.viala@femto-st.fr

Thiago de Paula Sales
Aeronautics Institute of Technology, Praça Marechal Eduardo Gomes, 50 – São José dos Campos, 12228-900, SP, Brazil
tpsales@ita.br, thiago.sales@gp.ita.br

Morvan Ouisse
Université Marie et Louis Pasteur, SUPMICROTECH, CNRS, Institut FEMTO-ST, Besançon, F-25000, France
morvan.ouisse@femto-st.fr

Abstract. *Periodic structures (PSs) have enabled vibration and noise reduction thanks to the so-called bandgaps (frequency ranges within which wave propagation is forbidden or strongly attenuated). The dynamic behavior of hydroelastic PSs (HPSs), i.e., lattices that combine elastic (solid) and fluid media, appears, however, to has received limited attention. In this work, PSs with 1D periodicity and box-like unit cells featuring 3D geometry are investigated. The hollow unit cells allow different fluid fillings within the cell cavities, enabling the assessment of the dynamic behavior of empty, partially filled, and fully filled PSs. Comprehensive numerical simulations and experiments show that fluid filling plays a crucial role in the wave propagation characteristics of the considered PSs, shifting bandgaps and creating additional frequency bands of wave suppression. The results of this research open new avenues for the design of advanced strategies and structures for wave manipulation, spanning applications from tunable bandgaps to smart and self-/adaptive devices.*

Keywords: *periodic structures, fluid–structure interaction, sloshing, model order reduction, wave finite element method.*

1. INTRODUCTION

The study of (quasi-)periodic structures (Q-PSs) has been motivated by various interesting functionalities they enable, including elastic and acoustic wave filtering through the so-called bandgaps (Elmadih *et al.*, 2021), waveguiding phenomena (Laude, 2021), wave/energy localization (Barbosa *et al.*, 2024), directional wave propagation (Li *et al.*, 2011), cloaking (Kadic *et al.*, 2020), etc. Such engineered systems frequently exhibit periodicity in one, two or three directions, where a single unit cell is spatially replicated to form the overall structure. Although considerable attention has been given to a variety of periodic media (Hussein *et al.*, 2014; Comandini *et al.*, 2025), *hydroelastic PSs* (HPSs) have been explored in few works. This class of periodic multiphysics lattices combines elastic and fluid domains in the unit cell architecture, as reflected in the term “hydroelastic”, where the prefix hydro, derived from the Greek, denotes water (*hydōr*).

Analogously to traditional PSs, HPSs can be broadly classified into (hydroelastic) phononic crystals (HPCs) and (hydro)elastic metamaterials (HEMs). Hydroelastic PCs are artificially engineered systems exhibiting material and/or geometric spatial periodicity. They are often designed to passively block the propagation of elastic and/or acoustic waves by exploiting the so-called *Bragg-scattering phenomenon*, which generates frequency bandgaps within which waves are forbidden to propagate. Since Bragg-scattering arises from periodic features in the unit cell, Bragg-type bandgaps typically occur at wavelengths comparable to the unit cell length, governed by the so-called *Bragg condition* (Xiao *et al.*,

This work is licensed under a Creative Commons “Attribution 4.0 International” license.

2012). This makes HPCs more suitable for wave manipulation at higher frequencies. On the other hand, HEMs embed one or more resonators in their unit cells, such that the *local resonance phenomenon* arises; thus, bandgaps are no longer restricted to higher frequencies. That is, bandgaps can be created by tuning the resonator natural frequency, for instance by altering its stiffness or inertia. Locally resonant bandgaps therefore emerge at subwavelength scale and are more suitable for lower-frequency applications (Claeys *et al.*, 2013). In practice, complex PSs rarely exhibit only one type of bandgap, since both Bragg-scattering and locally resonant effects can occur simultaneously (Jin *et al.*, 2022).

In this work, a PS exhibiting one-dimensional (1D) periodicity and featuring unit cells with 3D geometry is investigated, as shown in Fig. 1. Each box-like cuboid unit cell features an internal void that allows water filling at different levels, thereby enabling strong fluid–structure couplings not observed in the corresponding water-empty configuration, even though air remains present within the unit cell cavities. The baseline (empty) PS is, in reality, a simple PC-like beam whose periodicity generates Bragg-type bandgaps, as shown later.



Figure 1: Periodic structure with one-dimensional periodicity and box-like unit cells of three-dimensional geometry.

This type of PC was first investigated in a preliminary study, where evidence of improved dynamic behavior for vibration suppression was observed when the structure's cavities were completely filled with water (Santos *et al.*, 2023). The results showed that significant vibration reduction could be achieved in the water-filled PS at frequencies near the second Bragg-like bandgap of the baseline, fluid-empty PS. This outcome could not be explained at that time, as the numerical simulations considered only empty unit cells.

Later, simulations concerning wave dispersion and harmonic response analyses demonstrated that the incorporation of fluid within unit cell cavities increases the structure's inertia and, as a result, shift bandgaps and resonances toward lower frequencies (Santos *et al.*, 2024). This frequency shift enabled the generation of an additional Bragg-like bandgap within the analyzed frequency spectrum. The significant vibration reduction previously observed in the water-filled PS at frequencies near the second Bragg-like bandgap of the corresponding empty lattice has therefore been explained as a consequence of bandgap merging (Xiao *et al.*, 2023).

Although empty and fully filled PCs have been explored in the previous works, HPSs partially filled with water have only been addressed more recently (Santos *et al.*, 2025a). Since the fluid free-surface becomes unconstrained, complex sloshing phenomena arise. This topic was first investigated considering PSs exhibiting 1D periodicity and planar unit cell design. Numerical simulations showed that partially filled PSs allow the opening of additional bandgaps, not encountered in either empty or fully filled unit cell designs. Intermediate fluid levels therefore lead to non-trivial/unexpected dynamics, revealing that water filling does not alter only inertia. In addition, wave dispersion analyses demonstrated that the propagation of both elastic and acoustic waves can be inhibited by the incorporation of communicating channels between unit cells, due to simultaneous occurrence of elastic and fluid bandgaps.

The analysis of HPSs exhibiting box-like, three dimensional unit cells partially filled with water (Fig. 2) only came to light afterwards, where Santos *et al.* (2025c) investigated the impact of fluid filling on dynamic responses. Numerical simulations demonstrated that PSs partially filled with fluid display dynamic behavior markedly different from that of either empty or fully-filled structures. The results showed that partially filled PSs exhibit larger frequency bands with low-amplitude response, possibly resulting from bandgaps. In addition, the results indicated that wave propagation can be manipulated by exploiting different fluid fillings.

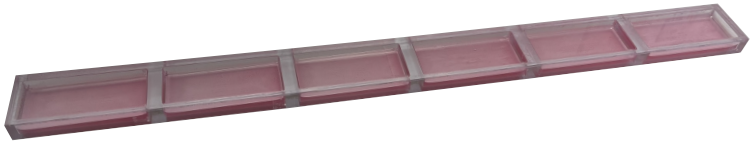


Figure 2: Periodic structure previously shown in Fig. 1, partially filled with water dyed red.

Although HPSs have been studied to some extent in the previous works, experimental investigations remain limited. Accordingly, this paper reports experimental results obtained recently to validate numerical findings. It also includes discussions of wave dispersion phenomena in empty, partially filled, and fully filled PSs. Simulations are performed using the so-called Wave-based Finite Element Method (WFEM), together with reduced-order unit cell models.

Beyond this introduction, the paper is organized as follows. First, Section 2 addresses the modeling of empty, partially filled, and fully filled PSs using reduced-order models and the WFEM. Next, Section 3 presents results from experiments and numerical simulations and discusses the wave propagation characteristics of the considered lattices. Finally, the conclusions of the work are summarized in Section 4, followed by the acknowledgment and reference sections.

2. MODELING

This section discusses the modeling of HPSs partially filled with fluid using reduced-order unit cell models and the WFEM. The analysis of empty and fully filled PSs can also be accommodated within the considered modeling framework, provided that appropriate modifications are taken into account.

2.1 Equations of motion for a single unit cell

The equations of motion for a single unit cell of a HPS, such as the system shown in Fig. 2, read as follows (Tran *et al.*, 2010):

$$\begin{bmatrix} \hat{\mathbf{M}}_{\mathrm{U}} & \mathbf{0} \\ \gamma\rho\,\hat{\mathbf{R}}^{\mathrm{T}} & \kappa\gamma(\hat{\mathbf{M}}_{\mathrm{P}}+\hat{\mathbf{M}}_{\mathrm{S}}) \end{bmatrix} \begin{Bmatrix} \ddot{\hat{\mathbf{q}}}_{\mathrm{U}} \\ \kappa^{-1}\ddot{\hat{\mathbf{q}}}_{\mathrm{P}} \end{Bmatrix} + \begin{bmatrix} \hat{\mathbf{K}}_{\mathrm{U}} & -\kappa\hat{\mathbf{R}} \\ \mathbf{0} & \kappa\gamma\hat{\mathbf{K}}_{\mathrm{P}} \end{bmatrix} \begin{Bmatrix} \hat{\mathbf{q}}_{\mathrm{U}} \\ \kappa^{-1}\hat{\mathbf{q}}_{\mathrm{P}} \end{Bmatrix} = \begin{Bmatrix} \hat{\mathbf{f}}_{\mathrm{U}} \\ \gamma\hat{\mathbf{f}}_{\mathrm{P}} \end{Bmatrix}, \tag{1}$$

where $\hat{\mathbf{q}}_{\mathrm{U}}$ and $\hat{\mathbf{q}}_{\mathrm{P}}$ gather structural (U) and fluid (P) DoFs, respectively; $\hat{\mathbf{f}}_{\mathrm{U}}$ and $\hat{\mathbf{f}}_{\mathrm{P}}$ are load vectors associated with $\hat{\mathbf{q}}_{\mathrm{U}}$ and $\hat{\mathbf{q}}_{\mathrm{P}}$, respectively; $\hat{\mathbf{M}}_j$ and $\hat{\mathbf{K}}_j$ ($j \in \{\mathrm{U}, \mathrm{P}\}$) denote respectively the inertia and stiffness matrices of structural (U) and fluid (P) domains; $\hat{\mathbf{M}}_{\mathrm{S}}$ is the sloshing mass matrix (Ansys®, 2024a); $\hat{\mathbf{R}}$ denotes the fluid–structure coupling matrix; ρ is the fluid density; κ and γ are constants used to improve the conditioning of the system matrices (Maess and Gaul, 2006); $(\ )^{\mathrm{T}}$ represents the transpose operator; and $(\ddot{\ })$ denotes second-order time derivatives.

Equation (1) can be organized with respect to the unit cell left (L), right (R), and internal (I) DoF locations ($\hat{\mathbf{q}}_{i_j}$, for $i \in \{\mathrm{U}, \mathrm{P}\}$ and $j \in \{\mathrm{L}, \mathrm{R}, \mathrm{I}\}$) and the fluid–structure interface Γ ($\hat{\mathbf{q}}_{\Gamma_j} = \{\hat{\mathbf{q}}^{\mathrm{T}}_{\Gamma_{j,\mathrm{U}}}\ \hat{\mathbf{q}}^{\mathrm{T}}_{\Gamma_{j,\mathrm{P}}}\}^{\mathrm{T}}$, for $j \in \{\mathrm{L}, \mathrm{R}, \mathrm{I}\}$):

$$\hat{\mathbf{M}}\ddot{\hat{\mathbf{q}}} + \hat{\mathbf{K}}\hat{\mathbf{q}} = \hat{\mathbf{f}}, \tag{2}$$

where:

$$\hat{\mathbf{q}} = \{\hat{\mathbf{q}}^{\mathrm{T}}_{\mathrm{U_L}}\ \ \hat{\mathbf{q}}^{\mathrm{T}}_{\mathrm{P_L}}\ \ \hat{\mathbf{q}}^{\mathrm{T}}_{\Gamma_{\mathrm{L}}}\ \ \hat{\mathbf{q}}^{\mathrm{T}}_{\mathrm{U_R}}\ \ \hat{\mathbf{q}}^{\mathrm{T}}_{\mathrm{P_R}}\ \ \hat{\mathbf{q}}^{\mathrm{T}}_{\Gamma_{\mathrm{R}}}\ \ \hat{\mathbf{q}}^{\mathrm{T}}_{\mathrm{U_I}}\ \ \hat{\mathbf{q}}^{\mathrm{T}}_{\mathrm{P_I}}\ \ \hat{\mathbf{q}}^{\mathrm{T}}_{\Gamma_{\mathrm{I}}}\}^{\mathrm{T}}, \tag{3}$$

$$\hat{\mathbf{f}} = \{\hat{\mathbf{f}}^{\mathrm{T}}_{\mathrm{U_L}}\ \ \hat{\mathbf{f}}^{\mathrm{T}}_{\mathrm{P_L}}\ \ \hat{\mathbf{f}}^{\mathrm{T}}_{\Gamma_{\mathrm{L}}}\ \ \hat{\mathbf{f}}^{\mathrm{T}}_{\mathrm{U_R}}\ \ \hat{\mathbf{f}}^{\mathrm{T}}_{\mathrm{P_R}}\ \ \hat{\mathbf{f}}^{\mathrm{T}}_{\Gamma_{\mathrm{R}}}\ \ \hat{\mathbf{f}}^{\mathrm{T}}_{\mathrm{U_I}}\ \ \hat{\mathbf{f}}^{\mathrm{T}}_{\mathrm{P_I}}\ \ \hat{\mathbf{f}}^{\mathrm{T}}_{\Gamma_{\mathrm{I}}}\}^{\mathrm{T}}. \tag{4}$$

2.2 Reduction of uncoupled structural and acoustic internal DoFs

The $\mathrm{U_I}$ and $\mathrm{P_I}$ DoF sets in Eq. (2) are uncoupled from each other, as they are separated by the fluid–structure interface Γ_{I}. Therefore, their reduction can be performed independently of the remaining sets of internal and boundary DoFs, using the Craig–Bampton method:

$$\hat{\mathbf{q}} = \boldsymbol{\alpha}_{\mathrm{CB}}\tilde{\mathbf{q}}, \tag{5}$$

where:

$$\tilde{\mathbf{q}} = \left\{\hat{\mathbf{q}}^{\mathrm{T}}_{\mathrm{U_L}}\ \ \hat{\mathbf{q}}^{\mathrm{T}}_{\mathrm{P_L}}\ \ \hat{\mathbf{q}}^{\mathrm{T}}_{\Gamma_{\mathrm{L}}}\ \ \hat{\mathbf{q}}^{\mathrm{T}}_{\mathrm{U_R}}\ \ \hat{\mathbf{q}}^{\mathrm{T}}_{\mathrm{P_R}}\ \ \hat{\mathbf{q}}^{\mathrm{T}}_{\Gamma_{\mathrm{R}}}\ \ \mathbf{q}^{\mathrm{T}}_{\mathrm{U_I}}\ \ \mathbf{q}^{\mathrm{T}}_{\mathrm{P_I}}\ \ \hat{\mathbf{q}}^{\mathrm{T}}_{\Gamma_{\mathrm{I}}}\right\}^{\mathrm{T}}, \tag{6}$$

$$\boldsymbol{\alpha}_{\mathrm{CB}} = \begin{bmatrix} \mathbf{I} & \mathbf{0} & \mathbf{0} & \mathbf{0} & \mathbf{0} & \mathbf{0} & \mathbf{0} & \mathbf{0} & \mathbf{0} \\ \mathbf{0} & \mathbf{I} & \mathbf{0} & \mathbf{0} & \mathbf{0} & \mathbf{0} & \mathbf{0} & \mathbf{0} & \mathbf{0} \\ \mathbf{0} & \mathbf{0} & \mathbf{I} & \mathbf{0} & \mathbf{0} & \mathbf{0} & \mathbf{0} & \mathbf{0} & \mathbf{0} \\ \mathbf{0} & \mathbf{0} & \mathbf{0} & \mathbf{I} & \mathbf{0} & \mathbf{0} & \mathbf{0} & \mathbf{0} & \mathbf{0} \\ \mathbf{0} & \mathbf{0} & \mathbf{0} & \mathbf{0} & \mathbf{I} & \mathbf{0} & \mathbf{0} & \mathbf{0} & \mathbf{0} \\ \mathbf{0} & \mathbf{0} & \mathbf{0} & \mathbf{0} & \mathbf{0} & \mathbf{I} & \mathbf{0} & \mathbf{0} & \mathbf{0} \\ \boldsymbol{\Sigma}_{\mathrm{U_I,U_L}} & \boldsymbol{\Sigma}_{\mathrm{U_I,P_L}} & \boldsymbol{\Sigma}_{\mathrm{U_I},\Gamma_{\mathrm{L}}} & \boldsymbol{\Sigma}_{\mathrm{U_I,U_R}} & \boldsymbol{\Sigma}_{\mathrm{U_I,P_R}} & \boldsymbol{\Sigma}_{\mathrm{U_I},\Gamma_{\mathrm{R}}} & \boldsymbol{\Xi}_{\mathrm{U_I}} & \mathbf{0} & \boldsymbol{\Sigma}_{\mathrm{U_I},\Gamma_{\mathrm{I}}} \\ \boldsymbol{\Sigma}_{\mathrm{P_I,U_L}} & \boldsymbol{\Sigma}_{\mathrm{P_I,P_L}} & \boldsymbol{\Sigma}_{\mathrm{P_I},\Gamma_{\mathrm{L}}} & \boldsymbol{\Sigma}_{\mathrm{P_I,U_R}} & \boldsymbol{\Sigma}_{\mathrm{P_I,P_R}} & \boldsymbol{\Sigma}_{\mathrm{P_I},\Gamma_{\mathrm{R}}} & \mathbf{0} & \boldsymbol{\Xi}_{\mathrm{P_I}} & \boldsymbol{\Sigma}_{\mathrm{P_I},\Gamma_{\mathrm{I}}} \\ \mathbf{0} & \mathbf{0} & \mathbf{0} & \mathbf{0} & \mathbf{0} & \mathbf{0} & \mathbf{0} & \mathbf{0} & \mathbf{I} \end{bmatrix}, \tag{7}$$

with $\mathbf{I}$ denoting identity matrices, and $\boldsymbol{\Sigma}$ and $\boldsymbol{\Xi}$ matrices of static modes and fixed-interface normal modes, respectively.

Using Eq. (5) in Eq. (2) and pre-multiplying the result by $\boldsymbol{\alpha}^{\mathrm{T}}_{\mathrm{CB}}$, partially reduced equations of motion can be derived:

$$\tilde{\mathbf{M}}\ddot{\tilde{\mathbf{q}}} + \tilde{\mathbf{K}}\tilde{\mathbf{q}} = \tilde{\mathbf{f}}, \tag{8}$$

where $\tilde{\mathbf{M}} = \boldsymbol{\alpha}^{\mathrm{T}}_{\mathrm{CB}}\hat{\mathbf{M}}\boldsymbol{\alpha}_{\mathrm{CB}}$, $\tilde{\mathbf{K}} = \boldsymbol{\alpha}^{\mathrm{T}}_{\mathrm{CB}}\hat{\mathbf{K}}\boldsymbol{\alpha}_{\mathrm{CB}}$ and $\tilde{\mathbf{f}} = \boldsymbol{\alpha}^{\mathrm{T}}_{\mathrm{CB}}\hat{\mathbf{f}}$. Although several equations are typically replaced by generalized DoFs in this step, the unit cell model may still contain a large number of physical DoFs, as the fluid-structure interfaces and boundary DoFs remain preserved; therefore, their reduction is addressed subsequently.

2.3 Reduction of coupled structural and acoustic internal DoFs

The Γ_{I} DoF set can be reduced locally using the following relation:

$$\tilde{\mathbf{q}} = \boldsymbol{\alpha}_{\text{L-CC}_{\Gamma_{\mathrm{I}}}}\bar{\mathbf{q}}, \tag{9}$$

where:

$$\bar{\mathbf{q}} = \left\{\hat{\mathbf{q}}_{\mathrm{U_L}}^{\mathrm{T}} \quad \hat{\mathbf{q}}_{\mathrm{P_L}}^{\mathrm{T}} \quad \hat{\mathbf{q}}_{\Gamma_{\mathrm{L}}}^{\mathrm{T}} \quad \hat{\mathbf{q}}_{\mathrm{U_R}}^{\mathrm{T}} \quad \hat{\mathbf{q}}_{\mathrm{P_R}}^{\mathrm{T}} \quad \hat{\mathbf{q}}_{\Gamma_{\mathrm{R}}}^{\mathrm{T}} \quad \mathbf{q}_{\mathrm{U_I}}^{\mathrm{T}} \quad \mathbf{q}_{\mathrm{P_I}}^{\mathrm{T}} \quad \mathbf{q}_{\Gamma_{\mathrm{I}}}^{\mathrm{T}}\right\}^{\mathrm{T}}, \tag{10}$$

$$\boldsymbol{\alpha}_{\text{L-CC}_{\Gamma_{\mathrm{I}}}} = \begin{bmatrix} \mathbf{I} & \mathbf{0} \\ \mathbf{0} & \boldsymbol{\Psi}_{\Gamma_{\mathrm{I}}} \end{bmatrix}, \tag{11}$$

with $\boldsymbol{\Psi}_{\Gamma_{\mathrm{I}}}$ denoting the adopted projection matrix.

The basis $\boldsymbol{\Psi}_{\Gamma_{\mathrm{I}}}$ can be obtained using three classes of Ritz vectors known as local modes (LMs), rigid body modes (RBMs), and low-frequency flexible body modes (FBMs), respectively collected into matrices $\mathbf{L}$, $\mathbf{R}$, and $\mathbf{F}$ (Herrmann *et al.*, 2010) — the later two collectively standing for global modes (GMs). The LMs and GMs are computed from matrix pencils $(\tilde{\mathbf{K}}_{\Gamma_{\mathrm{I}},\Gamma_{\mathrm{I}}}, \tilde{\mathbf{M}}_{\Gamma_{\mathrm{I}},\Gamma_{\mathrm{I}}})$ and $(\tilde{\mathbf{K}}, \tilde{\mathbf{M}})$, respectively. As unit cells of HPSs can be partially filled with fluid (cf. Fig. 2), rather than fully filled, sloshing modes (SMs) arise in the derivation of LMs and FBMs. Since the very low-eigenvalue SMs are numerous, they should not be indiscriminately included in $\boldsymbol{\Psi}_{\Gamma_{\mathrm{I}}}$; otherwise the MOR becomes inefficient. Accordingly, eigenvectors should be separated into SMs and non-SMs (N-SMs), such that:

$$\boldsymbol{\Psi}_{\Gamma_{\mathrm{I}}} = \left[\begin{array}{ccccc|ccccc} \overbrace{\cancel{\mathbf{L}_{\Gamma_{\mathrm{I,U}}}^{\mathrm{SMs}}}}^{\text{LMs}} & \overbrace{\mathbf{L}_{\Gamma_{\mathrm{I,U}}}^{\text{N-SMs}}}^{\text{LMs}} & \overbrace{\mathbf{R}_{\Gamma_{\mathrm{I,U}}}}^{\text{GMs}} & \overbrace{\cancel{\mathbf{F}_{\Gamma_{\mathrm{I,U}}}^{\mathrm{SMs}}}}^{\text{GMs}} & \overbrace{\mathbf{F}_{\Gamma_{\mathrm{I,U}}}^{\text{N-SMs}}}^{\text{GMs}} & \mathbf{0} & \mathbf{0} & \mathbf{0} & \mathbf{0} & \mathbf{0} \\ \mathbf{0} & \mathbf{0} & \mathbf{0} & \mathbf{0} & \mathbf{0} & \underbrace{\cancel{\mathbf{L}_{\Gamma_{\mathrm{I,P}}}^{\mathrm{SMs}}}}_{\text{LMs}} & \underbrace{\mathbf{L}_{\Gamma_{\mathrm{I,P}}}^{\text{N-SMs}}}_{\text{LMs}} & \underbrace{\mathbf{R}_{\Gamma_{\mathrm{I,P}}}}_{\text{GMs}} & \underbrace{\mathbf{F}_{\Gamma_{\mathrm{I,P}}}^{\text{SMs}}}_{\text{GMs}} & \underbrace{\mathbf{F}_{\Gamma_{\mathrm{I,P}}}^{\text{N-SMs}}}_{\text{GMs}} \end{array}\right], \tag{12}$$

where the crossed matrices refer to sets of eigenvectors that are removed from the projection basis.

Using Eq. (9) in Eq. (8) and pre-multiplying the result by $\boldsymbol{\alpha}_{\text{L-CC}_{\Gamma_{\mathrm{I}}}}^{\mathrm{T}}$ leads to:

$$\bar{\mathbf{M}}\ddot{\bar{\mathbf{q}}} + \bar{\mathbf{K}}\bar{\mathbf{q}} = \bar{\mathbf{f}}, \tag{13}$$

where $\bar{\mathbf{M}} = \boldsymbol{\alpha}_{\text{L-CC}_{\Gamma_{\mathrm{I}}}}^{\mathrm{T}} \tilde{\mathbf{M}} \boldsymbol{\alpha}_{\text{L-CC}_{\Gamma_{\mathrm{I}}}}$, $\bar{\mathbf{K}} = \boldsymbol{\alpha}_{\text{L-CC}_{\Gamma_{\mathrm{I}}}}^{\mathrm{T}} \tilde{\mathbf{K}} \boldsymbol{\alpha}_{\text{L-CC}_{\Gamma_{\mathrm{I}}}}$ and $\bar{\mathbf{f}} = \boldsymbol{\alpha}_{\text{L-CC}_{\Gamma_{\mathrm{I}}}}^{\mathrm{T}} \tilde{\mathbf{f}}$. For now, all interior DoFs of the unit cell model have been reduced to generalized/modal coordinates. The reduction of boundary DoFs, which may involve uncoupled structural and fluid DoFs, as well as fluid–structure coupled DoFs in the general case, is discussed in the next subsection.

2.4 Reduction of boundary DoFs

The unit cell boundary DoFs ($\mathrm{U_L}$, $\mathrm{P_L}$, Γ_{L}, $\mathrm{U_R}$, $\mathrm{P_R}$, and Γ_{R} DoF sets) can be reduced using local-level characteristic constraint (L-CC) MOR approach (Santos *et al.*, 2025b), for which the following relation applies:

$$\bar{\mathbf{q}} = \boldsymbol{\alpha}_{\text{L-CC}_{\mathrm{B}}} \mathbf{q}, \tag{14}$$

where:

$$\mathbf{q} = \left\{\mathbf{q}_{\mathrm{U_L}}^{\mathrm{T}} \quad \mathbf{q}_{\mathrm{P_L}}^{\mathrm{T}} \quad \mathbf{q}_{\Gamma_{\mathrm{L}}}^{\mathrm{T}} \quad \mathbf{q}_{\mathrm{U_R}}^{\mathrm{T}} \quad \mathbf{q}_{\mathrm{P_R}}^{\mathrm{T}} \quad \mathbf{q}_{\Gamma_{\mathrm{R}}}^{\mathrm{T}} \quad \mathbf{q}_{\mathrm{U_I}}^{\mathrm{T}} \quad \mathbf{q}_{\mathrm{P_I}}^{\mathrm{T}} \quad \mathbf{q}_{\Gamma_{\mathrm{I}}}^{\mathrm{T}}\right\}^{\mathrm{T}}, \tag{15}$$

$$\boldsymbol{\alpha}_{\text{L-CC}_{\mathrm{B}}} = \begin{bmatrix} \boldsymbol{\Psi}_{\mathrm{U_{LR}}} & \mathbf{0} & \mathbf{0} & \mathbf{0} & \mathbf{0} & \mathbf{0} & \mathbf{0} & \mathbf{0} & \mathbf{0} \\ \mathbf{0} & \boldsymbol{\Psi}_{\mathrm{P_{LR}}} & \mathbf{0} & \mathbf{0} & \mathbf{0} & \mathbf{0} & \mathbf{0} & \mathbf{0} & \mathbf{0} \\ \mathbf{0} & \mathbf{0} & \boldsymbol{\Psi}_{\Gamma_{\mathrm{LR}}} & \mathbf{0} & \mathbf{0} & \mathbf{0} & \mathbf{0} & \mathbf{0} & \mathbf{0} \\ \mathbf{0} & \mathbf{0} & \mathbf{0} & \boldsymbol{\Psi}_{\mathrm{U_{LR}}} & \mathbf{0} & \mathbf{0} & \mathbf{0} & \mathbf{0} & \mathbf{0} \\ \mathbf{0} & \mathbf{0} & \mathbf{0} & \mathbf{0} & \boldsymbol{\Psi}_{\mathrm{P_{LR}}} & \mathbf{0} & \mathbf{0} & \mathbf{0} & \mathbf{0} \\ \mathbf{0} & \mathbf{0} & \mathbf{0} & \mathbf{0} & \mathbf{0} & \boldsymbol{\Psi}_{\Gamma_{\mathrm{LR}}} & \mathbf{0} & \mathbf{0} & \mathbf{0} \\ \mathbf{0} & \mathbf{0} & \mathbf{0} & \mathbf{0} & \mathbf{0} & \mathbf{0} & \mathbf{I} & \mathbf{0} & \mathbf{0} \\ \mathbf{0} & \mathbf{0} & \mathbf{0} & \mathbf{0} & \mathbf{0} & \mathbf{0} & \mathbf{0} & \mathbf{I} & \mathbf{0} \\ \mathbf{0} & \mathbf{0} & \mathbf{0} & \mathbf{0} & \mathbf{0} & \mathbf{0} & \mathbf{0} & \mathbf{0} & \mathbf{I} \end{bmatrix}, \tag{16}$$

with $\boldsymbol{\Psi}_{\mathrm{U_{LR}}}$, $\boldsymbol{\Psi}_{\mathrm{P_{LR}}}$, and $\boldsymbol{\Psi}_{\Gamma_{\mathrm{LR}}}$ denoting augmented eigenvector matrices used for MOR, defined below.

The bases $\boldsymbol{\Psi}_{\mathrm{U_{LR}}}$ and $\boldsymbol{\Psi}_{\mathrm{P_{LR}}}$ are employed to project the $\mathrm{U_L}$, $\mathrm{P_L}$, $\mathrm{U_R}$, and $\mathrm{P_R}$ uncoupled DoF sets into modal coordinates. These projection matrices are derived from eigenvectors of the previously solved eigenproblem defined by the matrix pencil $(\tilde{\mathbf{K}}, \tilde{\mathbf{M}})$, so that no additional computational effort is required. Accordingly, $\boldsymbol{\Psi}_{\mathrm{U_{LR}}}$ and $\boldsymbol{\Psi}_{\mathrm{P_{LR}}}$ write as follows:

$$\boldsymbol{\Psi}_{\mathrm{U_{LR}}} = \left[\cancel{\tilde{\boldsymbol{\phi}}_{\mathrm{U_{L_1}}}^{\mathrm{SMs}}} \quad \cdots \quad \cancel{\tilde{\boldsymbol{\phi}}_{\mathrm{U_{L_\star}}}^{\mathrm{SMs}}} \quad \tilde{\boldsymbol{\phi}}_{\mathrm{U_{L_1}}}^{\text{N-SMs}} \quad \cdots \quad \tilde{\boldsymbol{\phi}}_{\mathrm{U_{L_\star}}}^{\text{N-SMs}} \quad \cancel{\tilde{\boldsymbol{\phi}}_{\mathrm{U_{R_1}}}^{\mathrm{SMs}}} \quad \cdots \quad \cancel{\tilde{\boldsymbol{\phi}}_{\mathrm{U_{R_\star}}}^{\mathrm{SMs}}} \quad \tilde{\boldsymbol{\phi}}_{\mathrm{U_{R_1}}}^{\text{N-SMs}} \quad \cdots \quad \tilde{\boldsymbol{\phi}}_{\mathrm{U_{R_\star}}}^{\text{N-SMs}}\right], \tag{17}$$

$$\boldsymbol{\Psi}_{\mathrm{P_{LR}}} = \left[\tilde{\boldsymbol{\phi}}_{\mathrm{P_{L_1}}}^{\mathrm{SMs}} \quad \cdots \quad \tilde{\boldsymbol{\phi}}_{\mathrm{P_{L_\star}}}^{\mathrm{SMs}} \quad \tilde{\boldsymbol{\phi}}_{\mathrm{P_{L_1}}}^{\text{N-SMs}} \quad \cdots \quad \tilde{\boldsymbol{\phi}}_{\mathrm{P_{L_\star}}}^{\text{N-SMs}} \quad \tilde{\boldsymbol{\phi}}_{\mathrm{P_{R_1}}}^{\mathrm{SMs}} \quad \cdots \quad \tilde{\boldsymbol{\phi}}_{\mathrm{P_{R_\star}}}^{\mathrm{SMs}} \quad \tilde{\boldsymbol{\phi}}_{\mathrm{P_{R_1}}}^{\text{N-SMs}} \quad \cdots \quad \tilde{\boldsymbol{\phi}}_{\mathrm{P_{R_\star}}}^{\text{N-SMs}}\right]. \tag{18}$$

where $\star$ denotes the number of retained eigenvectors in each eigenvector group. Crossed SMs are discarded.

On the other hand, the basis $\boldsymbol{\Psi}_{\Gamma_{\mathrm{LR}}}$ is used to project the Γ_{L} and Γ_{R} DoF sets, which exhibit coupled equations at each interface, into modal coordinates. This basis can be written similarly to Eq. (12), but grouping left and right eigenvectors so that Bloch–Floquet periodicity conditions are properly satisfied after MOR (Krattiger and Hussein, 2018):

$$\boldsymbol{\Psi}_{\Gamma_{\mathrm{LR}}} = \begin{bmatrix} \boldsymbol{\Psi}_{\Gamma_{\mathrm{LR\text{-}U}}} & \mathbf{0} \\ \mathbf{0} & \boldsymbol{\Psi}_{\Gamma_{\mathrm{LR\text{-}P}}} \end{bmatrix}, \tag{19}$$

where:

$$\boldsymbol{\Psi}_{\Gamma_{\mathrm{LR\text{-}U}}} = \Big[\overbrace{\cancel{\mathbf{L}^{\text{SMs}}_{\Gamma_{\mathrm{L,U}}}} \quad \mathbf{L}^{\text{N-SMs}}_{\Gamma_{\mathrm{L,U}}} \quad \cancel{\mathbf{L}^{\text{SMs}}_{\Gamma_{\mathrm{R,U}}}} \quad \mathbf{L}^{\text{N-SMs}}_{\Gamma_{\mathrm{R,U}}}}^{\text{LMs}} \quad \overbrace{\mathbf{R}_{\Gamma_{\mathrm{L,U}}} \quad \mathbf{R}_{\Gamma_{\mathrm{R,U}}} \quad \cancel{\mathbf{F}^{\text{SMs}}_{\Gamma_{\mathrm{L,U}}}} \quad \mathbf{F}^{\text{N-SMs}}_{\Gamma_{\mathrm{L,U}}} \quad \cancel{\mathbf{F}^{\text{SMs}}_{\Gamma_{\mathrm{R,U}}}} \quad \mathbf{F}^{\text{N-SMs}}_{\Gamma_{\mathrm{R,U}}}}^{\text{GMs}} \Big], \tag{20}$$

$$\boldsymbol{\Psi}_{\Gamma_{\mathrm{LR\text{-}P}}} = \Big[\overbrace{\cancel{\mathbf{L}^{\text{SMs}}_{\Gamma_{\mathrm{L,P}}}} \quad \mathbf{L}^{\text{N-SMs}}_{\Gamma_{\mathrm{L,P}}} \quad \cancel{\mathbf{L}^{\text{SMs}}_{\Gamma_{\mathrm{R,P}}}} \quad \mathbf{L}^{\text{N-SMs}}_{\Gamma_{\mathrm{R,P}}}}^{\text{LMs}} \quad \overbrace{\mathbf{R}_{\Gamma_{\mathrm{L,P}}} \quad \mathbf{R}_{\Gamma_{\mathrm{R,P}}} \quad \mathbf{F}^{\text{SMs}}_{\Gamma_{\mathrm{L,P}}} \quad \mathbf{F}^{\text{N-SMs}}_{\Gamma_{\mathrm{L,P}}} \quad \mathbf{F}^{\text{SMs}}_{\Gamma_{\mathrm{R,P}}} \quad \mathbf{F}^{\text{N-SMs}}_{\Gamma_{\mathrm{R,P}}}}^{\text{GMs}} \Big]. \tag{21}$$

In $\boldsymbol{\Psi}_{\Gamma_{\mathrm{LR\text{-}U}}}$ and $\boldsymbol{\Psi}_{\Gamma_{\mathrm{LR\text{-}P}}}$, LMs can be obtained from the local eigenvalue problems defined by matrix pencils $(\bar{\mathbf{K}}_{\Gamma_{\mathrm{L}},\Gamma_{\mathrm{L}}}, \bar{\mathbf{M}}_{\Gamma_{\mathrm{L}},\Gamma_{\mathrm{L}}})$ and $(\bar{\mathbf{K}}_{\Gamma_{\mathrm{R}},\Gamma_{\mathrm{R}}}, \bar{\mathbf{M}}_{\Gamma_{\mathrm{R}},\Gamma_{\mathrm{R}}})$. On the other hand, RBMs and low-frequency FBMs, which are part of GMs, are retrieved from the eigenvalue problem resulting from the matrix pencil $(\tilde{\mathbf{K}}, \tilde{\mathbf{M}})$, solved in the previous MOR step.

Pre-multiplying Eq. (13) by $\boldsymbol{\alpha}^{\mathrm{T}}_{\text{L-CC}_{\mathrm{B}}}$ and using Eq. (14) yields:

$$\mathbf{M}\ddot{\mathbf{q}} + \mathbf{K}\mathbf{q} = \mathbf{f}, \tag{22}$$

where $\mathbf{M} = \boldsymbol{\alpha}^{\mathrm{T}}_{\text{L-CC}_{\mathrm{B}}}\bar{\mathbf{M}}\boldsymbol{\alpha}_{\text{L-CC}_{\mathrm{B}}}$, $\mathbf{K} = \boldsymbol{\alpha}^{\mathrm{T}}_{\text{L-CC}_{\mathrm{B}}}\bar{\mathbf{K}}\boldsymbol{\alpha}_{\text{L-CC}_{\mathrm{B}}}$ and $\mathbf{f} = \boldsymbol{\alpha}^{\mathrm{T}}_{\text{L-CC}_{\mathrm{B}}}\bar{\mathbf{f}}$. At this point, all unit cell physical DoFs have been replaced by a set of modal coordinates, so that Eq. (22) can be used within the WFEM.

2.5 The Wave-based Finite Element Method

The application of the WFEM to HPSs whose unit cell models have been reduced according to Subsections 2.2, 2.3, and 2.4 is briefly discussed in this section. Further details on the WFEM can be found elsewhere (Mencik and Duhamel, 2015; Hoang *et al.*, 2020; Santos *et al.*, 2025b).

After deriving the reduced-order unit cell model given by Eq. (22), it must be cast in symmetric form, since the WFEM currently applies only to symmetric dynamic stiffness matrices to satisfy certain symplectic orthogonality conditions. This requirement may be fulfilled using an alternative formulation that replaces pressure DoFs by the so-called acoustic velocity potential φ (Everstine, 1981), such that the symmetric frequency-domain counterpart of Eq. (22) reads as follows:

$$\left(-\omega^2 \begin{bmatrix} \mathbf{M}_{\mathrm{U}} & \mathbf{0} \\ \mathbf{0} & -\rho\mathbf{M}_{\mathrm{P}} \end{bmatrix} + \mathrm{i}\,\omega \begin{bmatrix} \mathbf{0} & \rho\mathbf{R} \\ \rho\,\mathbf{R}^{\mathrm{T}} & \mathbf{0} \end{bmatrix} + \begin{bmatrix} \mathbf{K}_{\mathrm{U}} & \mathbf{0} \\ \mathbf{0} & -\rho\mathbf{K}_{\mathrm{P}} \end{bmatrix} \right) \begin{Bmatrix} \mathbf{Q}_{\mathrm{U}} \\ \mathbf{Q}_{\varphi} \end{Bmatrix} = \begin{Bmatrix} \mathbf{F}_{\mathrm{U}} \\ \mathbf{F}_{\varphi} \end{Bmatrix}, \tag{23}$$

where $\mathbf{Q}_{\mathrm{U}}$, $\mathbf{Q}_{\varphi}$, $\mathbf{F}_{\mathrm{U}}$, and $\mathbf{F}_{\varphi}$ respectively denote the frequency domain amplitudes associated with $\mathbf{q}_{\mathrm{U}}$, $\mathbf{q}_{\varphi}$, $\mathbf{f}_{\mathrm{U}}$ and $\mathbf{f}_{\varphi}$; ω is the circular frequency; and $\mathrm{i} = \sqrt{-1}$.

Dynamic condensation of internal DoFs of Eq. (23), followed by DoF compatibility and load equilibrium between (n) and $(n+1)$ unit cells of a lattice, leads to (Hoang *et al.*, 2020):

$$\mathbf{u}^{(n+1)}_{\mathrm{L}} = \mathbf{S}\mathbf{u}^{(n)}_{\mathrm{L}} + \mathbf{b}^{(n)}, \tag{24}$$

where $\mathbf{u}_{\mathrm{L}}$ is the state vector, $\mathbf{S}$ is the unit cell symplectic transfer matrix, and $\mathbf{b}$ is a vector of externally applied loads.

Setting $\mathbf{b}^{(n)} = \mathbf{0}$ in Eq. (24) and invoking the Bloch–Floquet theorem gives (Claro *et al.*, 2025):

$$\left(\mathbf{S} - \mu_j\mathbf{I}\right)\boldsymbol{\phi}_j = \mathbf{0}, \qquad \mu_j = \exp(-\mathrm{i}k_j\Delta), \qquad j \in \{1, \dots 2n_{\mathrm{B}}\}, \tag{25}$$

where μ_j and $\boldsymbol{\phi}_j$ are the wave mode pairs (propagation constants and wave shapes, respectively), k_j is the j-th Bloch wavenumber, Δ is the unit cell length in the direction of wave propagation, and n_{B} denotes the number of (modal) DoFs at the left or right interface of the unit cell.

Wave modes can be partitioned and organized according to the direction of wave propagation (Duhamel *et al.*, 2006):

$$\boldsymbol{\mu} = \mathrm{diag}(\mu_1,\ \dots,\ \mu_{n_{\mathrm{B}}}),\ \ \boldsymbol{\mu}^* = \mathrm{diag}(\mu^*_1,\ \dots,\ \mu^*_{n_{\mathrm{B}}}),\ \ \boldsymbol{\Phi} = \begin{bmatrix} \boldsymbol{\phi}_1 & \dots & \boldsymbol{\phi}_{n_{\mathrm{B}}} \end{bmatrix} = \begin{bmatrix} \boldsymbol{\Phi}_{\mathrm{Q}} \\ \boldsymbol{\Phi}_{\mathrm{F}} \end{bmatrix},\ \ \boldsymbol{\Phi}^* = \begin{bmatrix} \boldsymbol{\phi}^*_1 & \dots & \boldsymbol{\phi}^*_{n_{\mathrm{B}}} \end{bmatrix} = \begin{bmatrix} \boldsymbol{\Phi}^*_{\mathrm{Q}} \\ \boldsymbol{\Phi}^*_{\mathrm{F}} \end{bmatrix}, \tag{26}$$

where the superscript * refers to wave modes propagating from right to left, and subscripts Q and F identify partitions of $\boldsymbol{\Phi}$ and $\boldsymbol{\Phi}^*$ which are respectively associated with DoFs and loads.

Wave-mode expansion of $\mathbf{u}^{(n)}_{\mathrm{L}}$ and $\mathbf{b}^{(n)}$ can be shown to provide (Hoang *et al.*, 2020):

$$\mathbf{Q}^{(n)}_{\mathrm{L}} = \boldsymbol{\Phi}_{\mathrm{Q}}\boldsymbol{\mu}^{n-1}\mathbf{Q} + \boldsymbol{\Phi}^*_{\mathrm{Q}}\boldsymbol{\mu}^{N+1-n}\mathbf{Q}^* + \boldsymbol{\Phi}_{\mathrm{Q}}\sum\nolimits_{k=1}^{n-1}\boldsymbol{\mu}^{n-k-1}\mathbf{Q}^{(k)}_{\mathrm{B}} - \boldsymbol{\Phi}^*_{\mathrm{Q}}\sum\nolimits_{k=n}^{N}\boldsymbol{\mu}^{k+1-n}\mathbf{Q}^{*(k)}_{\mathrm{B}}, \tag{27}$$

$$-\mathbf{F}_{\mathrm{L}}^{(n)} = \boldsymbol{\Phi}_{\mathrm{F}}\boldsymbol{\mu}^{n-1}\mathbf{Q} + \boldsymbol{\Phi}_{\mathrm{F}}^{*}\boldsymbol{\mu}^{N+1-n}\mathbf{Q}^{*} + \boldsymbol{\Phi}_{\mathrm{F}}\sum_{k=1}^{n-1}\boldsymbol{\mu}^{n-k-1}\mathbf{Q}_{\mathrm{B}}^{(k)} - \boldsymbol{\Phi}_{\mathrm{F}}^{*}\sum_{k=n}^{N}\boldsymbol{\mu}^{k+1-n}\mathbf{Q}_{\mathrm{B}}^{*(k)}, \tag{28}$$

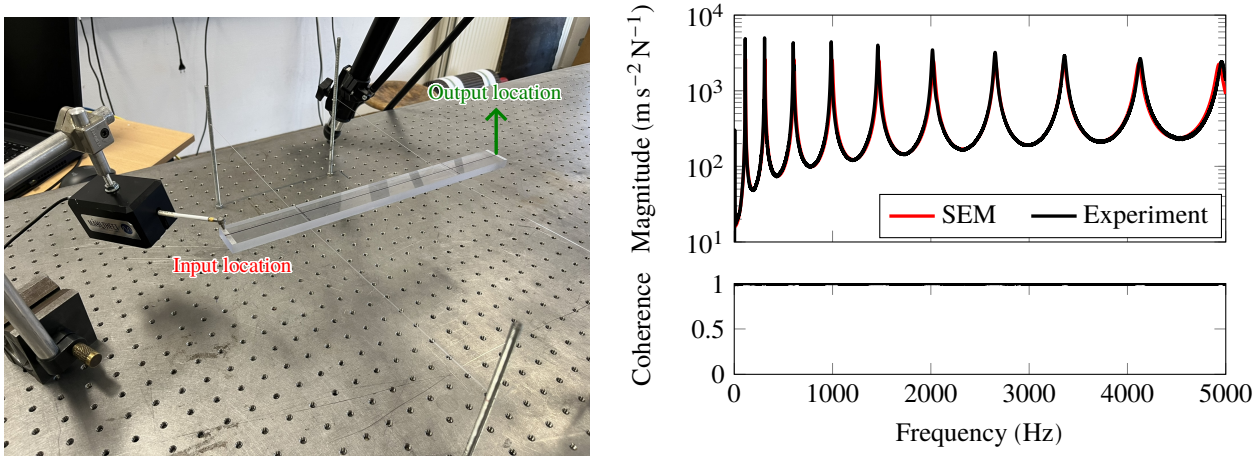
where N denotes the number of unit cells making up the PS; $\mathbf{Q}_{\mathrm{B}}$ and $\mathbf{Q}_{\mathrm{B}}^{*(k)}$ refer to wave mode amplitudes associated with external loads; and $\mathbf{Q}$ and $\mathbf{Q}^{*}$ represent wave mode amplitudes of waves that travel from the left boundary of the 1st cell to the right, and from the right boundary of the N-th cell to the left, respectively. Equations (27) and (28), along with boundary conditions, lead to a frequency-dependent linear system for $\mathbf{Q}$ and $\mathbf{Q}^{*}$. Structural ($\mathbf{Q}_{\mathrm{U}}$) and acoustic velocity potential ($\mathbf{Q}_{\varphi}$) amplitudes and/or loads ($\mathbf{F}_{\mathrm{U}}$, $\mathbf{F}_{\varphi}$) are subsequently computed, with pressure-like responses recovered as $\mathbf{Q}_{\mathrm{P}} = -\mathrm{i}\omega\rho\mathbf{Q}_{\varphi}$, both expressed in modal coordinates. Physical responses can then be retrieved by applying the frequency-domain counterpart of the transformation $\hat{\mathbf{q}} = \boldsymbol{\alpha}_{\mathrm{CB}}\boldsymbol{\alpha}_{\mathrm{L\text{-}CC}_{\Gamma_{\mathrm{I}}}}\boldsymbol{\alpha}_{\mathrm{L\text{-}CC}_{\mathrm{B}}}\mathbf{q}$ (cf. Subsections 2.2, 2.3, and 2.4).

3. RESULTS AND DISCUSSIONS

This section reports results obtained from numerical simulations and experimental investigations. First, the identification of polycarbonate material properties is addressed in Subsection 3.1. Then, the wave propagation characteristic of empty, partially filled, and fully filled PSs are examined in Subsection 3.2, which also discusses model verification (WFEM × FEM results) and model validation (WFEM × experiments).

3.1 Identification of polycarbonate material properties

Polycarbonate was selected to manufacture the PS introduced previously in Fig. 1. In order to determine the polycarbonate material properties, a homogeneous straight baseline beam with dimensions 360 mm × 30 mm × 9.70 mm was considered. The polycarbonate beam was subjected to an impact hammer test using the experimental setup presented in Fig. 3a, whose corresponding frequency response function (FRF) is provided in Fig. 3b (——). The polycarbonate density was calculated as 1200 kg m^{-3}, while its Poisson's ratio was taken from the literature as 0.38 (Faye *et al.*, 2014; Mullaoglu *et al.*, 2024). The spectral element method (SEM) was employed to derive the computational model of the polycarbonate beam (Lee, 2009). The SEM adopts frequency-dependent shape functions that exactly satisfy the governing equations of motion; consequently, its solution is exact, being limited only by the modeling assumptions themselves. In this work, the beam kinematics are described according to the Timoshenko beam theory. Accordingly, an FRF corresponding to the input and output locations shown in Fig. 3a was computed using the SEM, and the result is presented in Fig. 3b (——). The elastic modulus of polycarbonate was identified such that resonance frequencies predicted by the SEM and those observed experimentally in Fig. 3b match, for which a value of 2.65 GPa was found to provide very good agreement. In addition, dissipation effects were found to be important for polycarbonate; therefore, a hysteretic damping coefficient of 1.2% was adopted. In summary, the polycarbonate elastic modulus, density, Poisson's ratio, and hysteretic damping were defined as 2.65 GPa, 1200 kg m^{-3}, 0.38, and 1.2%, respectively.



(a) (b)

Figure 3: Preliminary test for the identification of the polycarbonate material properties: a) experimental setup (impact hammer test); and b) comparison between FRFs obtained from the SEM and experiment.

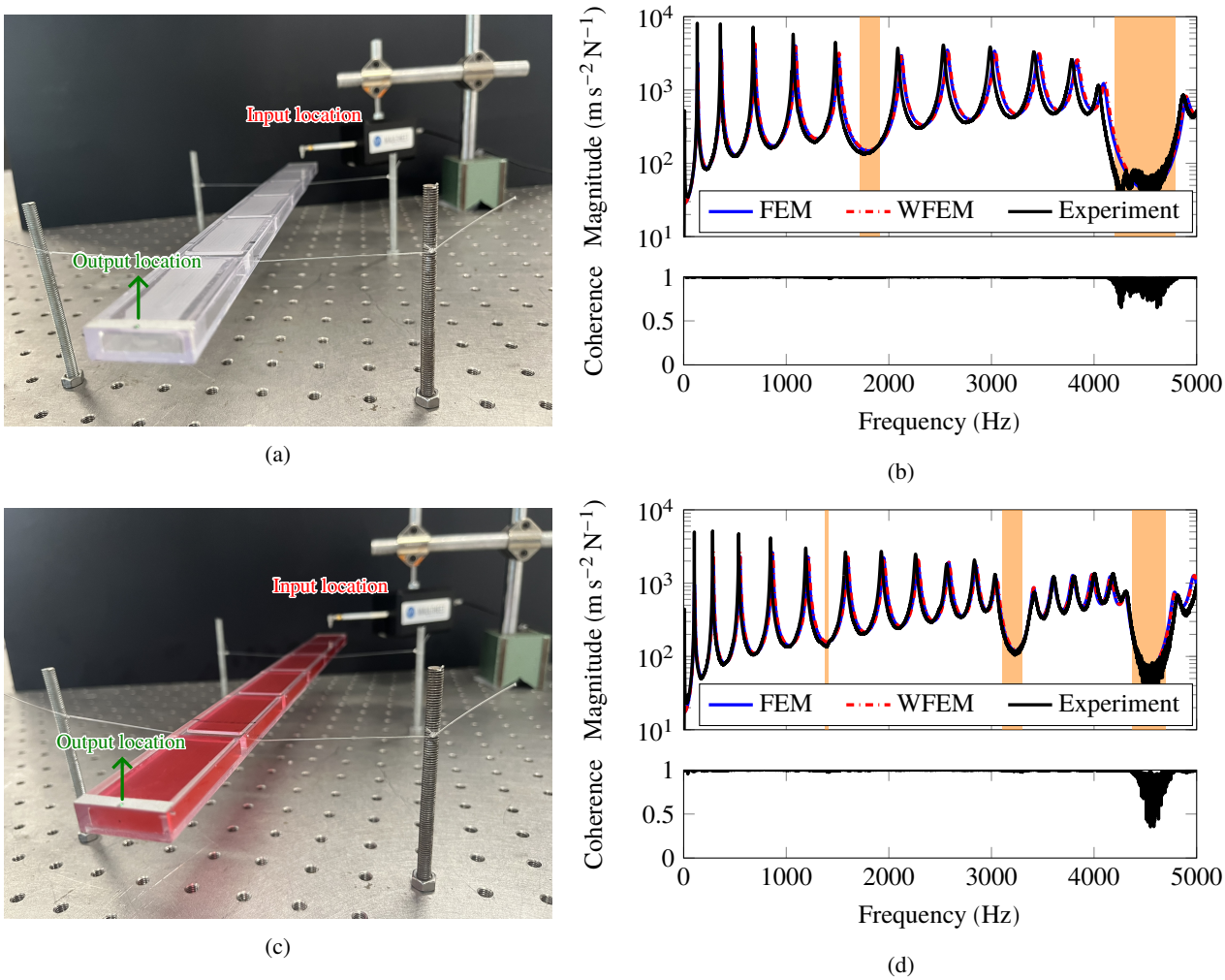
3.2 Wave propagation characteristics of empty, partially filled, and fully filled periodic structures

After identifying suitable values for the material properties of the polycarbonate specimen, the PS shown earlier in Fig. 1 was manufactured. In fact, the homogeneous straight beam previously shown in Fig. 3a was used in the machining process,

which introduced six identical, equally spaced cavities along its length, with dimensions 54 mm × 24.10 mm × 5.94 mm. Small lateral holes with a diameter of 1 mm were also manufactured in each cavity to allow different water fillings. Then, a cap with dimensions 357 mm × 26.84 mm × 1.88 mm was bonded to the machined beam using GreenPoxy 56 resin with SD 7561 hardener (Sicomin), resulting in the PS shown before in Fig. 1. Accordingly, Fig. 4 presents FRFs obtained from reference solutions (FEM), wave-based models (WFEM), and experiments (impact hammer tests) for empty and fully filled PSs. The same figure also highlights the frequency ranges for which $\mathrm{Im}\{k_j\} \neq 0$, determined considering null hysteretic damping. To account for the increase in mass due to the glue used to bond the cap to the machined beam, the polycarbonate density was updated to $1210\,\mathrm{kg\,m^{-3}}$. The water density and sound speed have been taken from the ANSYS material library, corresponding to $998.2\,\mathrm{kg\,m^{-3}}$ and $1482.1\,\mathrm{m\,s^{-1}}$, respectively (Ansys®, 2024b).

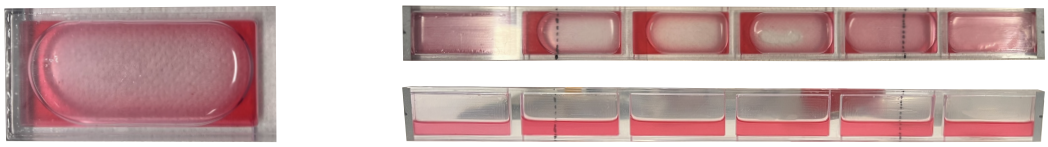
Figure 4 shows that FEM and WFEM results superpose, indicating that the wave-based models satisfactorily replace the cost-heavy FEM models. Recall that within the WFEM, meshing only a single unit cell of the lattice is necessary, which speeds up the analysis of PSs compared to the FEM. The results in Fig. 4 also show that the FRFs computed from WFEM/FEM are in very good agreement with the experimental results. Therefore, the coupled equations of motion presented earlier in Eq. (1), and the simplified version accounting only for structural DoFs, can be considered validated for predicting the dynamic response of the investigated PSs. Finally, it should be noted that frequency ranges for which wave propagation is forbidden in the FRFs shown in Fig. 4 closely match the bandgaps predicted by the Bloch–Floquet theorem.

Although the dynamic behavior of empty and fully filled PSs was examined in Fig. 4, there remains the need to investigate PSs whose unit cells are partially filled, for which sloshing phenomena might occur at the fluid free-surface. It turns out that the fluid free-surface does not remain perfectly flat in partially filled unit cells due to water surface tension, as shown in Fig. 5a. To circumvent this issue, ethanol was added to the water to reduce its surface tension and promote a nearly flat fluid free-surface. Top and lateral views of unit cells with increasing ethanol levels are depicted in Fig. 5b, which show that increasing the ethanol content in the water–ethanol mixture reduces the undesirable effects of surface tension, suppressing the formation of large bubbles within unit cells (Fig. 5b top) and mitigating meniscus development (Fig. 5b bottom) — the leftmost unit cell represents the optimal mixture configuration, exhibiting minimal surface tension effects.



(a) (b) (c) (d)

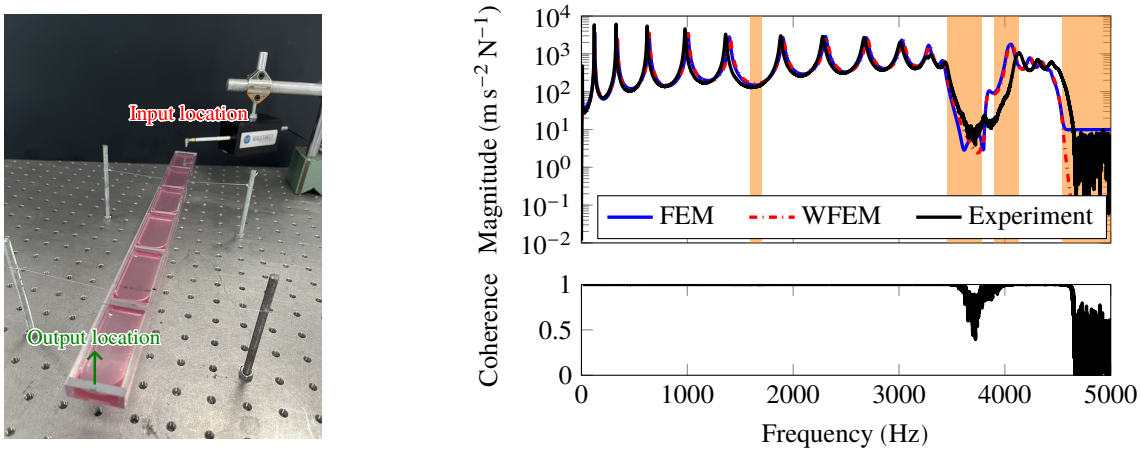
Figure 4: Experimental setups and FRFs for a HPS with internal cavities a–b) empty and c–d) fully filled.



(a) (b)

Figure 5: Surface tension issues in partially filled unit cells and their mitigation: a) bubble formation in a unit cell; b) influence of increasing ethanol on the fluid free-surface (the leftmost cell represents the optimal mixture configuration).

Due to the addition of ethanol to water, the resulting mixture density used in simulations was updated to 884 kg m^{-3} (the sound speed was kept constant, although it may have changed). Accordingly, Fig. 6 shows FRFs obtained from the FEM, WFEM, and the experiment for a PS partially filled with 1.98 mm of a water–ethanol mixture. The FRFs computed by FEM and WFEM closely match in Fig. 6b. Thus, the equation of motion presented earlier in Eq. (1) can accurately describe the dynamic behavior of partially filled unit cells, where sloshing phenomena might occur at the fluid free-surface. In addition, Fig. 6b shows that the bandgaps predicted using the Bloch-Floquet theorem, highlighted in orange, are in good agreement with frequency ranges with low vibration amplitude — the peak at 4065 Hz corresponds to a defect mode.



(a) (b)

Figure 6: Experimental setup (left) and FRFs (right) for a HPS with internal cavities 1.98 mm filled.

Although the water–ethanol mixture enabled the experiment presented previously in Fig. 6a to be carried out, tests involving PSs with higher fluid levels became more complicated due to capillary effects associated with fluid surface tension. As the unit cells approach a nearly-filled condition, the fluid tends to climb along the cavity walls, including the cap, leading to the formation of large, highly unstable trapped bubbles. This behavior was not observed for lower-filling levels, for which the fluid-free surface remained farther from the cap. To investigate this matter, Fig. 7 presents FRFs obtained for PSs filled to 3.96 mm, for which bubbles occur at arbitrary positions within the unit cells, namely left (L) or right (R).

The results in Fig. 7e show that bubble positions significantly influence the dynamic behavior of the PS, especially above 3000 Hz, where frequencies ranges with low vibration amplitudes can be observed. The FEM and WFEM results are in good agreement, once again demonstrating the wave-based model can replace cost-intensive FEM simulations. Since the numerical models do not account for the surface tension of the water–ethanol mixture, which leads to the formation of trapped bubbles within unit cells, the WFEM/FEM and experimental results do not match in Fig. 7e. Alternative numerical models could replace the simpler ones adopted in the WFEM/FEM modeling; however this was not pursued at this time.

To summarize, results in Figs. 4b, 4d, 6b, and 7e not only verified the WFEM models through FEM simulations, but also provide their experimental validation. The FRFs and wave dispersion analyses predicted by the Bloch–Floquet theorem demonstrate that wave propagation can be manipulated in PSs through different fluid fillings. Intermediate fluid levels reveal the opening of a larger number of bandgaps compared to empty or fully filled PSs. In addition, PSs partially filled with fluid exhibit dynamic behavior that is markedly distinct from the baseline empty and fully filled configurations, clearly showing that fluid filling does not correspond to a simple added-mass effect.

4. CONCLUDING REMARKS

This work investigated the dynamic behavior of PSs with 1D periodicity and box-like 3D unit cells. The hollow unit cells allowed different fluid fillings within their cavities, enabling the assessment of empty, partially filled, and fully

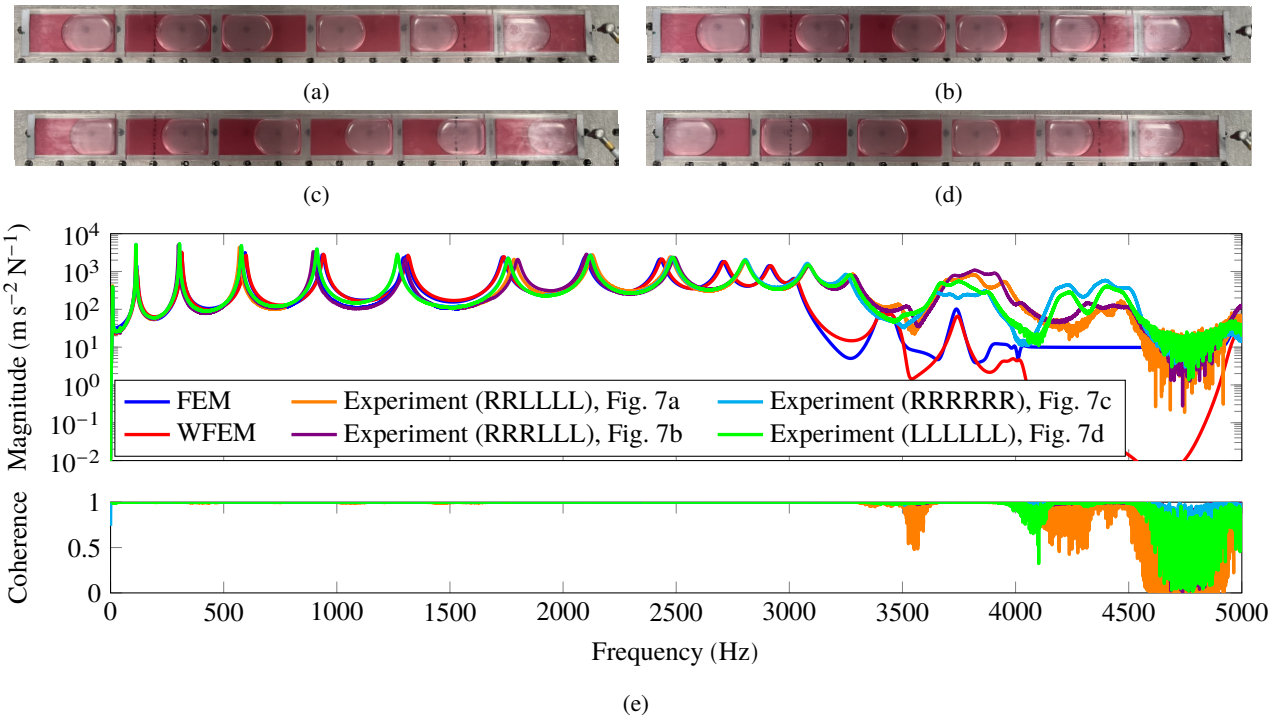


Figure 7: Vibration tests (impact hammer tests) performed on the beam-like PS with internal cavities 3.96 mm filled, with bubbles arbitrarily placed within unit cells, corresponding to a) RRLLLL; b) RRRLLL; c) RRRRRR; and d) LLLLLL locations.

filled configurations. Combined numerical–experimental analyses demonstrated that the reduced-order models and WFEM accurately predict the dynamic response and dispersion characteristics of the investigated PSs. Very good agreement among the FRFs computed using the WFEM, FEM, and experiments validated the wave-based formulation and derived reduced-order unit cell models, except for the PS with higher fluid filling, where surface tension effects were observed. The results revealed that fluid filling plays a crucial role in wave propagation, shifting bandgaps and creating additional frequency bands of wave suppression. This work therefore opens new avenues for the design of advanced structures featuring tunable dynamic properties by exploiting fluid–structure interaction, with great potential for vibration mitigation applications.

5. ACKNOWLEDGMENTS

This study was financed, in part, by the São Paulo Research Foundation (FAPESP), Brasil. Process Numbers #2018/15894-0, #2023/11207-7 and #2024/07549-2. All authors are grateful to FAPESP for the provided grants. V. M. S. Santos also acknowledges the Brazilian Coordination for the Improvement of Higher Education Personnel (CAPES). M. Ouisse acknowledges the graduate school EIPHI (project ANR-17-EURE-0002).

6. REFERENCES

Ansys®, 2024a. “Mechanical APDL 2024 R2, Release 24.2, Theory Reference, Acoustic Fluid-Structure Interaction (FSI), ANSYS, Inc.”

Ansys®, 2024b. “Workbench 2024 R1, Engineering data, Engineering data sources, Water liquid, ANSYS, Inc.”

Barbosa, A., Kacem, N. and Bouhaddi, N., 2024. “A design methodology for nonlinear oscillator chains enabling energy localization tuning and soliton stability enhancement with optimal damping”. *Mech. Syst. Signal Pr.*, Vol. 213, p. 111358. doi:10.1016/j.ymssp.2024.111358.

Claeys, C.C., Vergote, K., Sas, P. and Desmet, W., 2013. “On the potential of tuned resonators to obtain low-frequency vibrational stop bands in periodic panels”. *J. Sound Vib.*, Vol. 332, No. 6, pp. 1418–1436. doi:10.1016/j.jsv.2012.09.047.

Claro, D.S., Denis, V. and Mencik, J.M., 2025. “A wave finite element approach for the vibroacoustic analysis of fluid-filled pipes with joints and defects”. *Wave Motion*, Vol. 138, p. 103576. doi:10.1016/j.wavemoti.2025.103576.

Comandini, G., Ouisse, M., Ting, V.P. and Scarpa, F., 2025. “Architected acoustic metamaterials: An integrated design perspective”. *Appl. Phys. Rev.*, Vol. 12, No. 1. doi:10.1063/5.0230888.

Duhamel, D., Mace, B.R. and Brennan, M.J., 2006. “Finite element analysis of the vibrations of waveguides and periodic structures”. *J. Sound Vib.*, Vol. 294, No. 1–2, pp. 205–220. doi:10.1016/j.jsv.2005.11.014.

Elmadih, W., Chronopoulos, D. and Zhu, J., 2021. "Metamaterials for simultaneous acoustic and elastic bandgaps". *Sci. Rep.*, Vol. 11, No. 1. doi:10.1038/s41598-021-94053-3.

Everstine, G.C., 1981. "A symmetric potential formulation for fluid-structure interaction". *J. Sound Vib.*, Vol. 79, No. 1, pp. 157–160. doi:10.1016/0022-460x(81)90335-7.

Faye, A., Parmeswaran, V. and Basu, S., 2014. "Mechanics of Dynamic Fracture in Polycarbonate". *Procedia Mater. Sci.*, Vol. 3, pp. 1304–1309. doi:10.1016/j.mspro.2014.06.211.

Herrmann, J., Maess, M. and Gaul, L., 2010. "Substructuring including interface reduction for the efficient vibro-acoustic simulation of fluid-filled piping systems". *Mech. Syst. Signal Pr.*, Vol. 24, No. 1, pp. 153–163. doi:10.1016/j.ymssp.2009.05.003.

Hoang, T., Duhamel, D. and Foret, G., 2020. "Wave finite element method for waveguides and periodic structures subjected to arbitrary loads". *Finite Elem. Anal. Des.*, Vol. 179, p. 103437. doi:10.1016/j.finel.2020.103437.

Hussein, M.I., Leamy, M.J. and Ruzzene, M., 2014. "Dynamics of Phononic Materials and Structures: Historical Origins, Recent Progress, and Future Outlook". *Appl. Mech. Rev.*, Vol. 66, No. 4. doi:10.1115/1.4026911.

Jin, Y., Jia, X.Y., Wu, Q.Q., He, X., Yu, G.C., Wu, L.Z. and Luo, B., 2022. "Design of vibration isolators by using the Bragg scattering and local resonance band gaps in a layered honeycomb meta-structure". *J. Sound Vib.*, Vol. 521, p. 116721. doi:10.1016/j.jsv.2021.116721.

Kadic, M., Wegener, M., Nicolet, A., Zolla, F., Guenneau, S. and Diatta, A., 2020. "Elastodynamic behavior of mechanical cloaks designed by direct lattice transformations". *Wave Motion*, Vol. 92, p. 102419. doi:10.1016/j.wavemoti.2019.102419.

Krattiger, D. and Hussein, M.I., 2018. "Generalized Bloch mode synthesis for accelerated calculation of elastic band structures". *J. Comput. Phys.*, Vol. 357, pp. 183–205. doi:10.1016/j.jcp.2017.12.016.

Laude, V., 2021. "Principles and properties of phononic crystal waveguides". *APL Mater.*, Vol. 9, No. 8. doi:10.1063/5.0059035.

Lee, U., 2009. *Spectral Element Method in Structural Dynamics*. Wiley.

Li, X.F., Ni, X., Feng, L., Lu, M.H., He, C. and Chen, Y.F., 2011. "Tunable Unidirectional Sound Propagation through a Sonic-Crystal-Based Acoustic Diode". *Phys. Rev. Lett.*, Vol. 106, No. 8, p. 084301. doi:10.1103/physrevlett.106.084301.

Maess, M. and Gaul, L., 2006. "Substructuring and model reduction of pipe components interacting with acoustic fluids". *Mech. Syst. Signal Pr.*, Vol. 20, No. 1, pp. 45–64. doi:10.1016/j.ymssp.2005.02.008.

Mencik, J.M. and Duhamel, D., 2015. "A wave-based model reduction technique for the description of the dynamic behavior of periodic structures involving arbitrary-shaped substructures and large-sized finite element models". *Finite Elem. Anal. Des.*, Vol. 101, pp. 1–14. doi:10.1016/j.finel.2015.03.003.

Mullaoglu, F., Usta, F. and Turkmen, H.S., 2024. "The impact-induced deformation characteristics of polycarbonate panels". *Polym. Eng. Sci.*, Vol. 64, No. 6, pp. 2579–2593. doi:10.1002/pen.26711.

Santos, V.M.S., Sales, T.P. and Ouisse, M., 2023. "Investigation of a novel metastructure with trapped, fluid-filled unit cells". In *27th Int. Congr. Mech. Eng.* pp. 1–10. doi:10.26678/ABCM.COBEM2023.COB2023-1067.

Santos, V.M.S., Sales, T.P. and Ouisse, M., 2024. "Evaluation of wave propagation in fluid-filled, acoustic-structural phononic crystal using the wave-based finite element method, combined with a model order reduction scheme". In *XII Congr. Nac. Eng. Mec.* pp. 1–10. doi:10.26678/ABCM.CONEM2024.CON24-1559.

Santos, V.M.S., Sales, T.P. and Ouisse, M., 2025a. "Dynamic behavior of acousto-elastic phononic crystals incorporating fluid sloshing and communicating channels between unit cells". In *Proc. XX Int. Symp. Dynamic Probl. Mech.* pp. 1–10. doi:10.26678/ABCM.DINAME2025.DIN2025-0100.

Santos, V.M.S., Sales, T.P. and Ouisse, M., 2025b. "Improving the computation of forced responses of periodic structures by the wave-based finite element method via a modified generalized Bloch mode synthesis". *Finite Elem. Anal. Des.*, Vol. 245, No. 104314, p. 104314. doi:10.1016/j.finel.2025.104314.

Santos, V.M.S., Viala, R., Sales, T.P. and Ouisse, M., 2025c. "On the Wave Propagation in Hydroelastic Phononic Crystals". In *Proc. Int. Conf Struct. Eng. Dyn.* pp. 1–10.

Tran, Q.H., Ouisse, M. and Bouhaddi, N., 2010. "A robust component mode synthesis method for stochastic damped vibroacoustics". *Mech. Syst. Signal Pr.*, Vol. 24, No. 1, pp. 164–181. doi:10.1016/j.ymssp.2009.06.016.

Xiao, L., Bursi, O.S., Wang, M., Nagarajaiah, S., Sun, F. and Du, X.L., 2023. "Metamaterial beams with negative stiffness absorbers and rotation: band-gap behavior and band-gap merging". *Eng. Struct.*, Vol. 280, p. 115702. doi:10.1016/j.engstruct.2023.115702.

Xiao, Y., Wen, J. and Wen, X., 2012. "Longitudinal wave band gaps in metamaterial-based elastic rods containing multi-degree-of-freedom resonators". *New J. Phys.*, Vol. 14, No. 3, p. 033042. doi:10.1088/1367-2630/14/3/033042.

7. RESPONSIBILITY NOTICE

The authors are solely responsible for the printed material included in this paper.